Seamless tungsten disulfide-tungsten heterojunction with abundant exposed active sites for efficient hydrogen evolution

Jing Li[a,b], Wenting Hong[a,b,c,1], Chuanyong Jian[a,b], Qian Cai[a,b], Wei Liu[a,b,*]

[a] CAS Key Laboratory of Design and Assembly of Functional Nanostructures, Fujian Institute of Research on the Structure of Matter, Chinese Academy of Sciences, Fuzhou, 350002, China
[b] Fujian Provincial Key Laboratory of Nanomaterials, Fujian Institute of Research on the Structure of Matter, Chinese Academy of Sciences, Fuzhou, 350002, China
[c] University of Chinese Academy of Sciences, Beijing, 100049, China

A B S T R A C T

In this work, we report a simple bottom-up approach to synthesize seamless tungsten disulfide (WS_2)-tungsten (W) heterojunction electrode for efficient hydrogen evolution reaction (HER). Through one step sulfidation of WO_3/W, ultra-thin vertically-arranged WS_2 flakes with high surface areas and stepped-structure as well as abundant defects can grow on the W substrate. The synthesized WS_2/W electrode exhibits outstanding HER activity with an onset overpotential of as small as approximately 30 mV, and an operating potential of only 108 mV for 10 mA/cm^2, which is close to the state-of-the-art transition metal dichalcogenides (TMDs) HER electrocatalyst reported in the literature so far. The abundant exposed edges and defects of WS_2 along with excellent electrical contact between WS_2 and W substrate contribute to the high HER activity of WS_2/W electrode reported in this work.

1. Introduction

As clean and renewable energy, hydrogen (H_2) is a promising substitute for natural fossil fuels which give rise to the increasing global greenhouse effects [1,2]. Exploring environmentally sustainable H_2 energy technologies becomes an urgent need to solve the global environmental crisis. It is well known that the generation of hydrogen from water splitting is an attractive method [3,4]. The activity of electrocatalysts mainly determines the efficiency of H_2 production. So far, the most efficient and stable electrocatalysts for HER are platinum (Pt)-group metals [5,6]. However, their applications in large scale is severely restricted by the scarcity and high costs. It is highly desirable to explore earth abundant and inexpensive catalysts as suitable substitutes of Pt [7–11]. Recently, transition-metal dichalcogenides (TMDs), such as XS_2 (X = Mo, W) as well as its derivatives have attracted numerous attentions due to the potential of replacing Pt for electrochemical hydrogen generation [12–18]. Among them, molybdenum disulfide (MoS_2) is the one that gets the most attention and has been deeply studied as a HER catalyst. As the analogos of MoS_2, tungsten disulfide (WS_2) has the similar properties and exhibits promising electrocatalytic activity. Up till now, WS_2 has been synthesized

in forms of nanoparticles [19], nanoribbons [20], and nanosheets [21–24] using various methods for HER. It is well known that increasing the exposed edge sites and conductivity of WS_2 can boost the HER performance. On the other hand, the electrical contact between WS_2 and substrate also affects the electrocatalytic HER performance. Tour et al., reported the preparation of vertically aligned WS_2 nanosheets with abundant active edges by using a lithium-based anodization electrolyte to fabricate WO_3 films followed by sulfurization [25]. Chen and her colleagues have synthesized 3D hybrids of WS_2/graphene/Ni foam, in which graphene/Ni foam possess good conductivity and high surface area [26]. Wang et al., designed the rational WS_2/WO_x heterostructures grown on the graphite paper to boost the HER performance of WS_2 [27]. However, the large contact resistance between WS_2 or WS_2/WO_3 and conducting substrate still exists and will influence the HER performance. Compared with various complicated post-treatment means, the synthesis of vertical-oriented ultra-thin WS_2 with excellent conductivity on conducting substrate through simple methods can provide sufficient active sites for efficient HER.

In this study, we develop the WS_2 electrocatalyst grown on the W foil through a bottom-up fabrication approach, as illustrated in Fig. 1a. The W foil was oxidized in the air to expose larger surface areas and
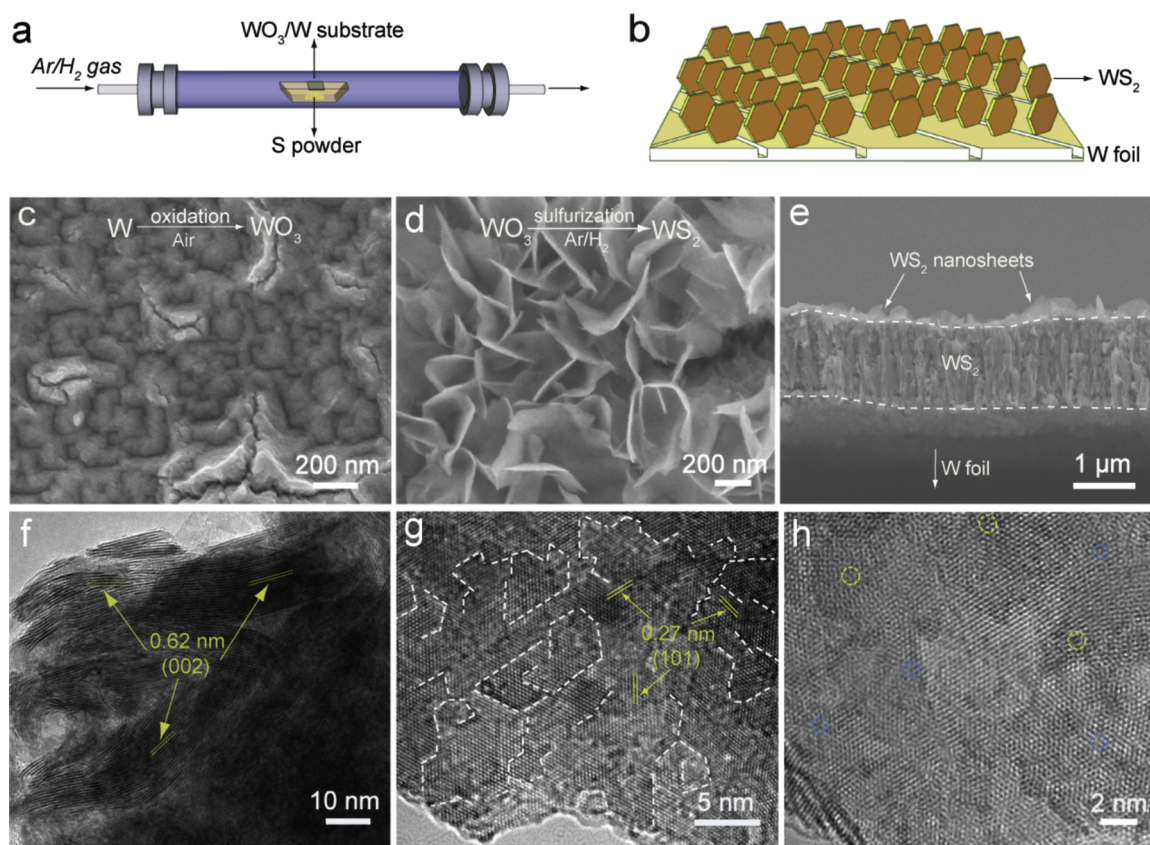
Fig. 1. (a) Schematic of WS$_2$ synthesis process. (b) The structural diagram of WS$_2$/W. SEM image of (c) WO$_3$ and (d) WS$_2$ nnaosheets on W foil. (e) Side-view SEM image of WS$_2$/W. (f) TEM image of edges of WS$_2$. (g, h) HRTEM images of the basal plane of WS$_2$. (i, j) The simulated (HAADF) images of WS$_2$ with W and S vacancies. The white dash lines in (g) mean the exposed edge sites and stepped structure of WS$_2$. The yellow and blue spheres in h1 ~ h3 (scale bar, 1nm) represent S and W atoms, the circular regions marked with yellow and red dash lines in h1 ~ h3 and i, j denote the S and W vacancy, respectively.

followed by the sulfurization in the Ar and H$_2$, during which process vertical WS$_2$ flakes can be synthesized in the W substrate (Fig. 1b). WS$_2$ can form a seamless electrical contact with electron collection substrate to completely remove the impact of the contact resistance on the HER performance. WS$_2$ nanosheets formed on W substrate at high temperature possess high-quality crystal structure, which enhances the conductivity of WS$_2$. In addition, there are also W, and S vacancies exist in the resulted structure that could provide more actives sites for the HER. The design of this high-performance WS$_2$ is also supported by density functional theory (DFT) calculation, which proves that W foil can form chemical bonds with WS$_2$, allowing electron transport without a barrier. In addition, W and S vacancies formed during the growth of WS$_2$ can introduce new gap states and more catalytic sites, therefore reducing the hydrogen adsorption free energy (ΔG_H). Undoubtedly, the proposed vertically arranged WS$_2$ nanosheets exhibits improved HER activity compared with most of the WS$_2$ reported in the previous literature. The resulted WS$_2$/W electrocatalyst exhibits outstanding HER activity with an overpotential of as small as approximately 30 mV, and an operating potential of only 108 mV for 10 mA/cm^2.

2. Experimental section

2.1. Materials synthesis

2.1.1. Oxidation of W foil

Before oxidation, high purity of W foil was ultrasonically cleaned in acetone, ethanol, and water for 15 min in sequence. A piece of clean W foil was placed on an empty alumina boat which was laid up in the center of a 2-inch diameter quartz tube furnace. The reactions are performed at the temperature of 450 °C with the heating rate of 20 °C/

min for 60 min in air and cool down to the room temperature naturally.

2.1.2. Preparation of WS$_2$/W electrocatalyst

WS$_2$ was grown on WO$_3$/W by vapor deposition synthesis using solid S powder precursor ($\geq$99.5%, 100 mg). An alumina boat with 100 mg S powder was loaded in the center zone of a 2-inch diameter quartz-tube furnace. The WO$_3$/W foil as both of the substrate and W source was placed directly on the boat. The temperature of the zone was raised to 600 °C at a speed of 30 °C/min and maintained for 40 min with the flow of 30 sccm Ar and 15 sccm H$_2$. After growth, the system was cooled down to room temperature naturally.

2.2. Electrochemical measurement

The electrocatalytic HER performance of various electrocatalysts are tested by a typical three-electrode system on an electrochemical workstation (CHI 660E). The linear sweep voltammetry scans from 0 to −0.8 V (vs. Ag/AgCl) with a sweep rate of 5 mV/s is conducted in 0.5 mol/L H$_2$SO$_4$ (pH = 0) electrolyte using Ag/AgCl (in 3.8 mol/L KCl solution) electrode as the reference electrode and graphite is taken as the counter electrode. The as-prepared samples serve as the working electrodes. Potentials in the article are referenced to a reversible hydrogen electrode (RHE). The long-term stability tests were performed by continuous cyclic voltammetry test in 0.5 mol/L H$_2$SO$_4$ at a scan rate of 200 mV/s and the time dependence of the current density at −0.2 V vs RHE for 10 h.

3. Results and discussion

3.1. Morphology, phase, and structure analysis of catalysts

W foils are utilized as both substrate and W source to prepare WS_2 electrode. The morphology and catalytic activity of WS_2 are determined by the surface treatment method of W foil. The synthesis of vertical ultra-thin WS_2 nanosheets on W foil is achieved through a simple two-step annealing method (Experimental Section). The top-view scanning electron microscopy (SEM) images (Figs. 1c–e, and S1) exhibit the different morphologies of W foil after different treatments. The morphologies of WO_3 and W foil are shown in Figs. 1c and S1a, respectively. The irregular WO_3 structures are formed on the surface of W foil after a simply annealing at 450 °C in the air, which can contribute to the form of WS_2 with large surface areas. When the sulfurization is performed on WO_3/W substrate, vertically-arranged thin WS_2 nanosheets can grow on the substrate (Figs. 1d and S1b). It's apparent that vertically-arranged WS_2 nanosheets have abundant edges, which could help improve the activity of HER. The side-view SEM image of WS_2/W foil is displayed in Fig. 1e, in which the ultra-thin WS_2 nanosheets can be also observed.

Transmission electron microscopy (TEM) and high-resolution TEM (HRTEM) can further investigate the structure of WS_2 nanosheets. The low-magnification TEM images in Fig. 1f reveals that the flakes have a layer structure with an interlayer spacing distance of 0.62 nm, corresponding to the (002) plane of WS_2 [28,29]. In addition, S-W-S layers with a layer-to-layer spacing of 0.27 nm in the high-magnification TEM image (Fig. 1g) belongs to the (101) facets of the WS_2. In the basal plane of WS_2 flakes, there are many exposed edges and stepped structure of WS_2 (white dash line, Fig. 1g) due to the variation of the number of layers formed during the growth of WS_2. Hence, the number of exposed edge sites of WS_2 is further increased. Besides, at high-magnification TEM image (Fig. 1h), the hexagonal structure of WS_2 can be observed, indicating that the ultra-thin WS_2 flakes synthesized by the sulfurization have high crystal quality. The defects and vacancy in the hexagonal structure can be observed in Fig. 1h1~h3, the yellow and red dash lines represent S and W vacancy, as depicted in Fig. S2a and b. The absence of S and W atoms caused the distortion of the chemical bond, which can be seen clearly from Fig. 1h1~h3, in which the S and W is arranged disorderly. In addition, the Dr. Probe method is used to simulate High-Angle Annular Dark Field (HAADF) images of WS_2 with S and W vacancies [30], as shown in Fig. 1i and j. The circular regions marked with yellow and red dash lines denote the S and W vacancy, respectively. In addition, the energy dispersive X-ray spectroscopy (EDS) in Fig. S3 reveal the presence and homogeneous distribution of S and W elements in the WS_2/W.

The conversion from WO_3 to WS_2 can be proved by the XRD patterns shown in Fig. 2a. After oxidizing of W foil, two distinct peaks at 23° and 33°corresponding to the (002) and (022) planes, indicating the formation of WO_3. By sulfurization of WO_3/W foil, the presence of WS_2 can be identified from the peaks at the 2θ value of 14.2°, 28.5° and 43.7°, which are all indexed to the WS_2 according to JCPDS card no. 08-0237 [25,28]. Raman spectra are also employed to examine the WO_3/W and WS_2/W substrate shown in Fig. 2b. For the WO_3, three peaks located at 813, 714 and 272 cm^{-1} correspond to the stretching of O−W−O, the stretching of W−O, and the bending of O−W−O, respectively [31,32]. As for the WS_2 nanosheets formed by the sulfidation of the WO_3/W, The peaks at 356 and 422 cm^{-1} can be assigned to the E_{2g}^1 mode (the in-plane W-S phonon mode) and A_{1g} mode (the out-of-plane W-S phonon mode) of WS_2. Besides, the small second-order peak at 297 cm^{-1} is attributed to the mode of 2LA(M)-2E_{2g}^2(M) [33–35]. XPS analysis is carried out to investigate the chemical states of prepared samples. Fig. S4 shows the XPS survey full spectrum of the WS_2/W, from which C, W, S and O elements are detected. In Fig. 2c, the two pronounced peaks observed at 33.1 eV (W $4f_{7/2}$) and 35.2 eV (W $4f_{5/2}$) are assigned to the W^{4+}, while the peak at 38.8 eV belongs to the

orbital of W^{4+} $5p_{3/2}$ [36,37]. Moreover, the S^{2-} $2p_{3/2}$ and S^{2-} $2p_{1/2}$ signals are discovered at 162.7 eV and 163.9 eV in the spectra of S 2p (Fig. 2d) [38]. The analysis of W and S confirmed the presence of WS_2. The depth profile of WS_2/W is also studied by ion milling and XPS spectra (Fig. 2e and f). The strong peak of WS_2 can be observed without ion milling. While the intensity of WS_2 peaks is reduced with the ion milling time increasing. Meanwhile, the intensity of WO_3 peak decreases and almost disappeared, implying that the sulfurization is mainly conducted on WO_3 in the surface of W foil.

3.2. Electrochemical characterization

A three-electrode system is utilized to analyze the HER activity of the samples with 0.5 M H_2SO_4 solution as the electrolyte. The commercial Pt/C (20 wt% Pt/XC-72) is also measured under the same condition for comparison. The linear sweep voltammograms (LSV) curves for the W foil, WO_3/W, and WS_2/W are shown in Fig. 3a. Apparently, both of pristine W foil and WO_3/W exhibit weak HER activity. After sulfurization of WO_3/W at 600 °C, WS_2/W electrocatalyst shows the best catalytic performance, exhibiting an onset potential of 30 mV and the potential of only 108 mV to reach the current density of 10 mA/cm^2, which is much smaller than WO_3/W and W foil. HER activity of WS_2/W hybrid synthesized under different reaction conditions is shown in Fig. 3b and c, which reveals that the oxidation and sulfurization temperatures of W foil play important roles in the HER activity of the of WS_2 flakes. 450 °C is selected as the optimal W oxidation temperature (Fig. 3b). Along with the increase the sulfurization temperatures above 600 °C, the HER activity of WS_2 decreases due to the reduction of defects which response for the HER activity (Fig. 3c). The oxidation process of W can increase the roughness of W foil, thereby increasing the active sites. One can conclude that the electrocatalyst displays the best performance when the temperature of W oxidation and sulfurization is performed at 450 °C and 600 °C, respectively.

Tafel polarization curves are plotted in Fig. 3d to further understand the HER mechanism of WS_2 nanosheets on W substrate. The Tafel slope of WO_3/W is estimated to be 81.4 mV per decade. After sulfurization of WO_3/W into the vertically-arranged WS_2 nanosheets which have a large amount of exposed catalytic surface area, a Tafel slope as small as of 45.5 mV/dec is obtained. The lowest Tafel slope of WS_2/W hybrid catalyst demonstrates the highest HER speed and favorable kinetics that benefit from many exposed active sites. Moreover, the value of 45.5 mV/dec also indicates that the rate determining step can be identified as the electrochemical desorption Heyrovsky step during the HER.

Besides, a useful technique of electrochemical impedance spectroscopy (EIS) is conducted to study the interface reactions and electrode kinetics in HER process. The typical Nyquist plots of the EIS response to various samples are obtained as depicted in Fig. S5a. It's obvious that WS_2/W has the smallest charge transfer resistance due to the key factor of fast electron transfer between the substrate and the catalytic edge sites of WS_2 that could devote to the superior HER kinetics. In addition, the Nyquist plots of WS_2/W are recorded at different potentials of -0.3 V ~ -0.38V (Fig. S5b). WS_2/W electrode exhibits one capacitive semicircle in the high frequencies zone at all applied potentials, suggesting that the corresponding equivalent circuit (inset of Fig. S5a) for HER is featured by one time constant and the reaction is kinetically controlled. WS_2 with better HER activity have a smaller resistance than that of W foil, which may be ascribed to the fast electron transfer rate between the catalytic center of WS_2 and W substrate. In addition, the Nyquist plots of WS_2/W recorded at different potentials (-0.30 V ~ -0.38 V) are shown in Fig. S5b. To estimate the electrochemically effective surface area of different catalysts, the capacitance of the double layer (C_{dl}) is determined by cyclic voltammetry measurements in 0.5 M H_2SO_4 solution [39]. C_{dl} can be extracted from the slope of the fitted lines of the plots in the figure of Δj against the cyclic voltammetry scan rates (Fig. S6), where Δj is derived by subtracting the negative current
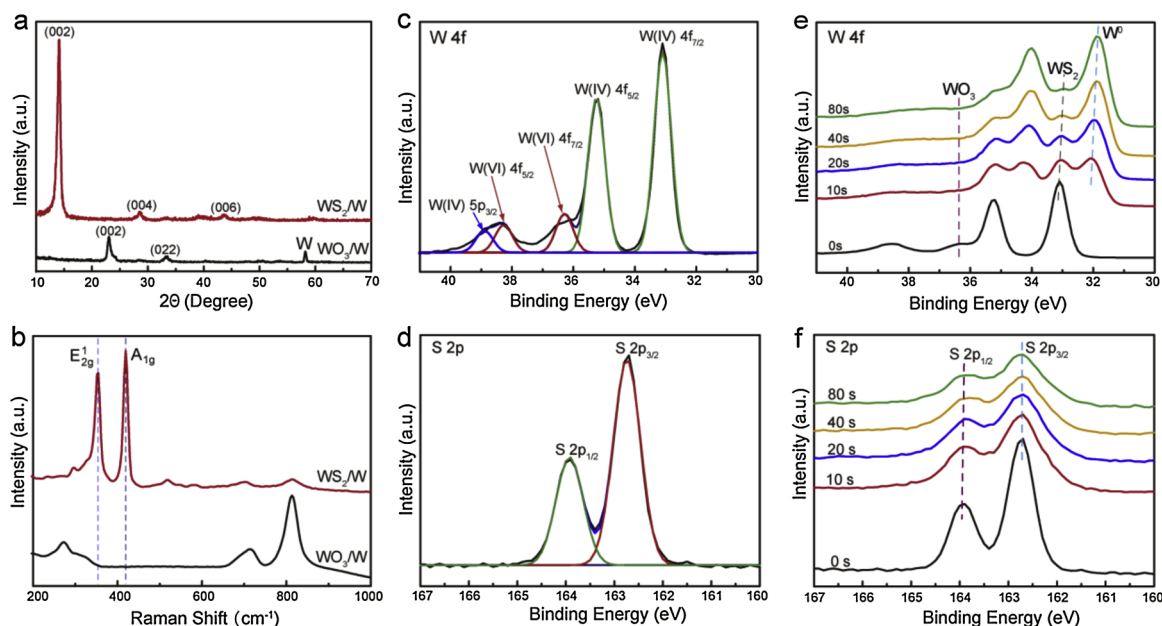
Fig. 2. (a) XRD patterns and (b) Raman spectra of WS$_2$ nanosheets and WO$_3$ grown on W foils. (c) XPS spectra of W 4f and (d) S 2p. The XPS depth profiles spectra of (e) W 4f and (f) S 2p about the WS$_2$.
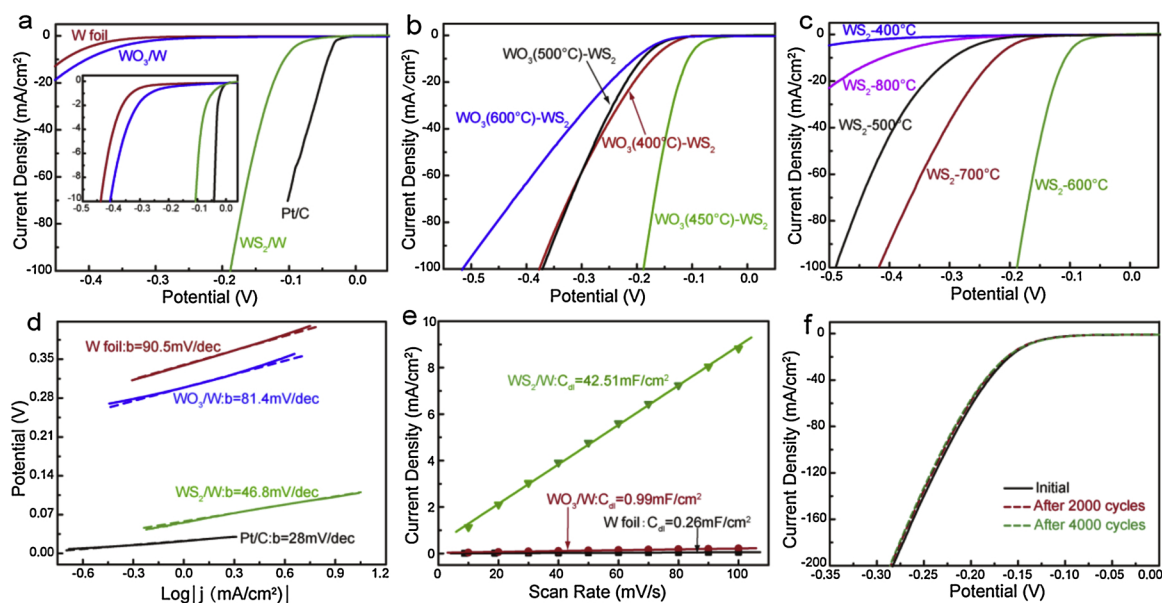
Fig. 3. (a) Polarization curves of W foil, WO$_3$/W, WS$_2$/W and commercial Pt/C catalysts measured in 0.5 M H$_2$SO$_4$ solution. Inset is the corresponding polarization curves recorded from the generation of current to the current density up to 10 mA/cm^2. (b) The polarization curves of WS$_2$ synthesized under various oxidation conditions: W foils are annealed in air at 400, 450, 500 and 600 °C, respectively. The sulfurization temperature of WO$_3$/W is 600 °C. (c) Sulfurization temperature (400–800 °C) of WO$_3$ effect on the HER performance of WS$_2$/W electrode. (d) The corresponding Tafel plots of different catalysts. (e) Current density variation at a given potential of 0.15 V vs RHE plotted against scan rate fitted to a linear regression enables the C$_{dl}$ estimation. (f) Polarization curves recorded from WS$_2$/W before (black curve) and after 2000 cycles (red curve) as well as 4000 cycles (green curve) of cyclic voltammetry test at a scan rate of 0.2 V/s. (For interpretation of the references to colour in this figure legend, the reader is referred to the web version of this article.)

density from the positive current density (j_a-j_c) at a given potential of 0.15 V versus RHE. As shown in Fig. 3e, C$_{dl}$ of W foil is of only 0.26 m F/cm^2, while the C$_{dl}$ values are calculated to be 0.99 m F/cm^2 and 42.51 m F/cm^2 for WO$_3$/W and WS$_2$/W, respectively. Hence, WS$_2$/W has the highest active sites among various samples. With the purpose of comparing the HER kinetics with the WS$_2$-based catalysts that are of highly active performance, the overpotentials required to generate a current density of 10 mA/cm^2 of the active WS$_2$-based catalysts are listed in Table S1. The HER activity of WS$_2$/W catalyst in this work is better than most of the active HER electrocatalysts in acidic solution.

Stability is another essential property of an electrocatalyst in evaluating the HER performance. In this work, continuous cyclic voltammetry test is carried out to acquire the long-term stability of WS$_2$/W in 0.5 M H$_2$SO$_4$. Compared with its original activity, there is negligible degradation of cathodic current densities for WS$_2$/W electrocatalyst after 2000 cycles, and even after 4000 cycles (Fig. 3f). The durability of WS$_2$/W electrode is also studied using amperometric i–t curve conducted at −0.2 V vs. RHE, as displayed in the inset figure of current (i)-time (t) curve in Fig. S7. The electrocatalyst demonstrates excellent stability with less than 14% degradation of the initial current after
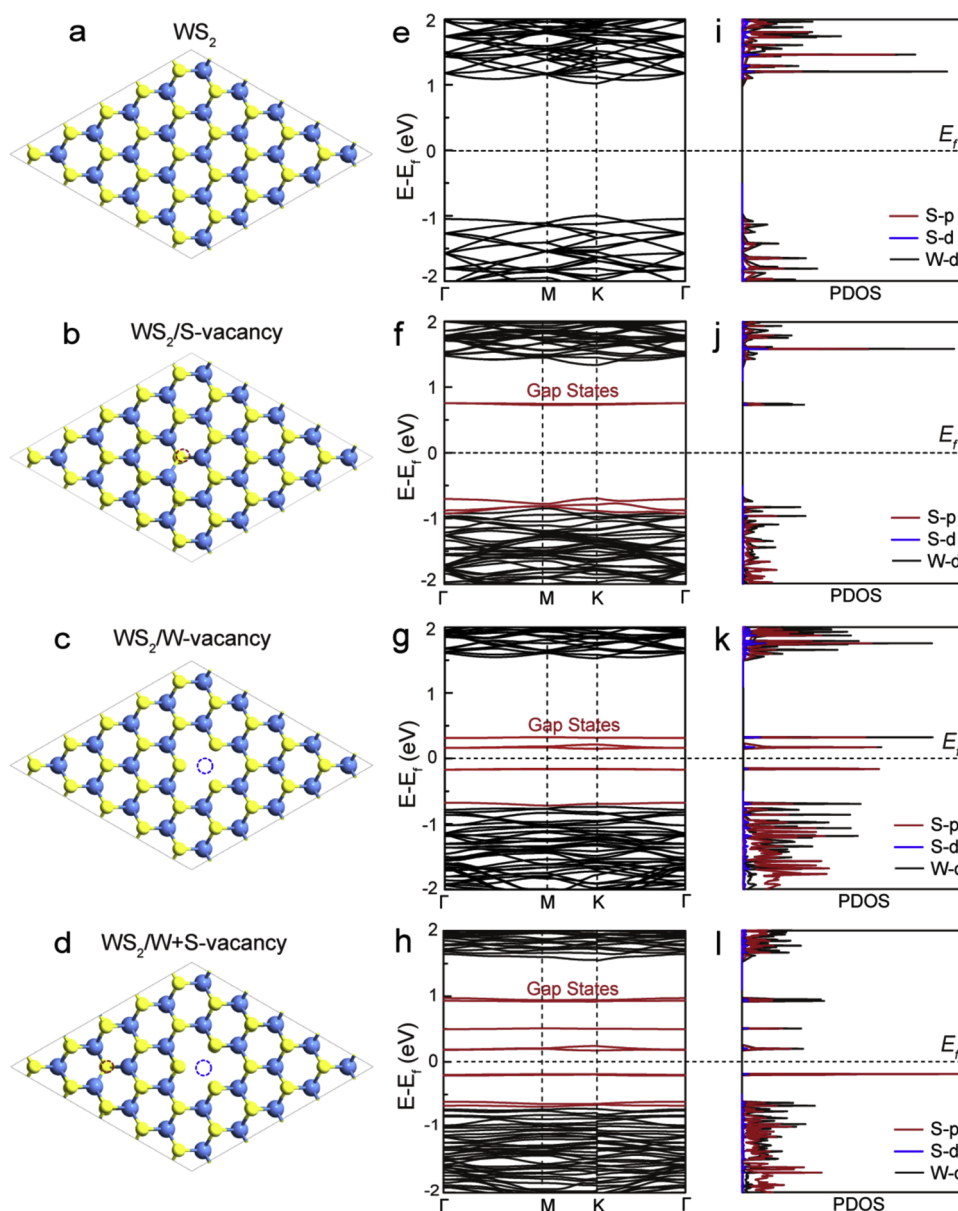
Fig. 4. Unit cells of (a) pristine WS$_2$, (b) a 5 × 5 WS$_2$ cell with one S vacancy, (c) a 5 × 5 WS$_2$ cell with a W vacancy, and (d) a 5 × 5 WS$_2$ cell with one S vacancy and one W vacancy. The circular region marked with red and blue dash lines denote the S and W vacancy, respectively. The yellow and blue spheres represent S and W atoms, respectively.(e–h) The corresponding band structures and (i–l) partial density of states (PDOS) plots of the WS$_2$ with various structures in (a-d). (For interpretation of the references to colour in this figure legend, the reader is referred to the web version of this article.)

operation for 10 h, exhibiting its potential application in the process of H$_2$ production.

3.3. DFT calculation

DFT calculation is utilized to explore the impact of the S and W vacancy on the electronic structure of WS$_2$. The structural diagrams of pristine WS$_2$ and WS$_2$ with different forms of defects (S or/and W vacancy) are shown in Fig. 4a–d. The corresponding band structure and PDOS is displayed in Fig. 4e–h and 4i–l. When the S or W vacancy is introduced into the WS$_2$ crystal structure(5 × 5 cell), there are new bands appear in the gap near the Fermi level (red curves in Fig. 4f–h). The increasing number of gap states can also be seen in the PDOS plots, which could result in the strengthening of hydrogen bonding, thereby reducing the ΔG_H and leading to the improvement of HER performance of WS$_2$.

As the edge of WS$_2$ is the main activity center, in which WS$_2$ is terminated by (10-10) W-edge and (-1010) S-edge. DFT calculation is carried out to compare the ΔG_H of WS$_2$ with flat-structure and stepped-structure.The result reveals that the ΔG_H of S-edge and W-edge is -3,61 eV and 3.47 eV of WS$_2$ film with flat structure, which is much smaller than that of the basal plane (ΔG_H = 8.50 eV) of WS$_2$ (Fig. 5a). The synthesized WS$_2$ film has many stepped edges, which have been observed by HRTEM shown in Fig. 1g. The ΔG_H of WS$_2$ with stepped structure (Fig. 5b right) is calculated to be -0.11 eV for S-edge, 0.43 eV for W-edge, and 1.35 eV for the basal plane (Fig. 5a). The corresponding structural schematic illustration of WS$_2$ with different structures is displayed in Fig. 5b, in which the stepped structure ensures optimal ΔG_H and ultrafast electron transport to the stepped WS$_2$ edge surface. Compared with the flat WS$_2$, the exposed edge of stepped WS$_2$ contributes much more to HER.

The difference between the superposed atomic valence density and self-consistent charge density is known as the electron difference density (EDD). The charge transfers from one atom to another would result
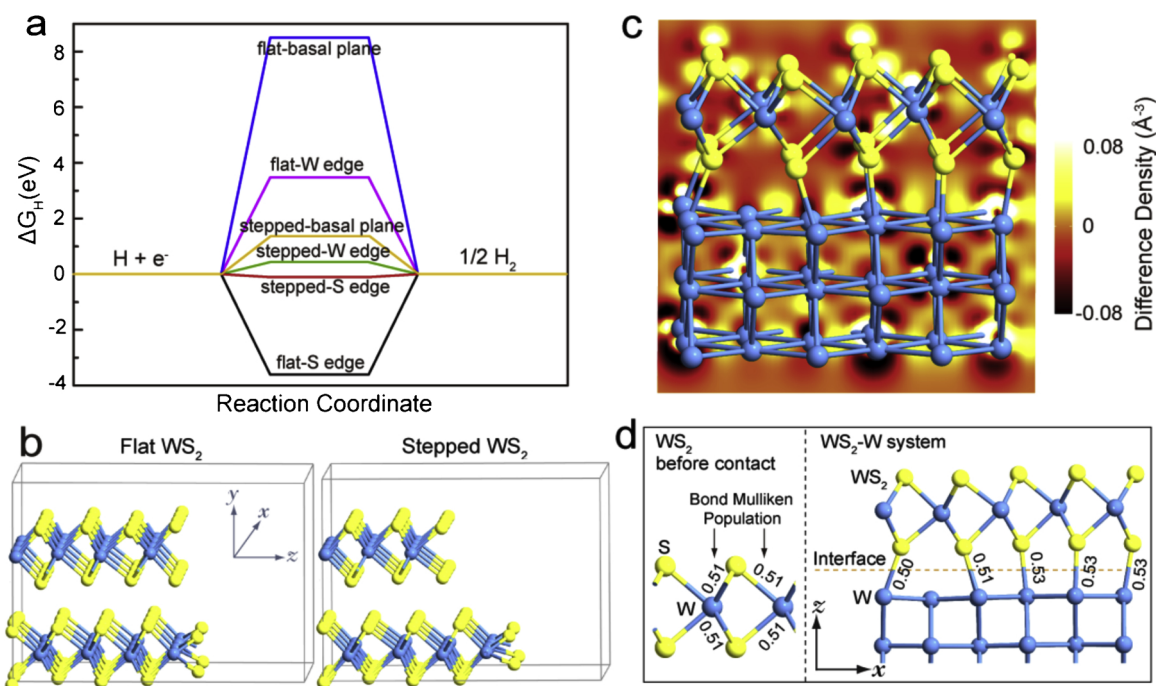
Fig. 5. (a) Free Gibbs energy diagram for hydrogen adsorption at various WS$_2$ basal planes and edges, in which the W edge has 50% S coverage. (b) The structural schematic illustration of flat and stepped WS$_2$ with sufficient vacuum on z direction. (c) Electron differential density (EDD) contour of the interface between WS$_2$ and W foil. The yellow and blue spheres represent S and W atoms, respectively. (d) Bond Mulliken population of W—S bonds in pristine WS$_2$ before contact (left) and W—S bonds at WS$_2$-W contact interface (right). (For interpretation of the references to colour in this figure legend, the reader is referred to the web version of this article.)

in a positive EDD on the charge acceptor and a negative EDD on the donor [40]. Fig. 5c shows the EDD contours of a hypothetical hexagonal WS$_2$ structure with exposing W and S edges applied with W layer. The S atoms have negative EDD sign while the W atoms have positive EDD, besides, there is a big region of positive EDD at the S–W bonds, which facilitate electrons transfer from S atoms to W atoms. The above results indicate the WS$_2$ could form a chemical bond with the W substrate and pose strong orbital overlaps at the interface to allow the electrons transfer easily from W substrate to WS$_2$. The bond Mulliken population (the overlap population of electrons for pairs of atomic orbitals) analysis is employed to confirm the orbital overlaps [41]. As shown in Fig. 5d, the population of every W—S bond in intrinsic WS$_2$ (left) and at the WS$_2$-W interface (right) is marked. The populations at the interface vary from 0.50 to 0.53, most of the values can be higher than that of the intrinsic WS$_2$ (0.51), implying that stronger covalent bonds can be formed at the interfaces between W and WS$_2$. Therefore, the abundant edges of WS$_2$ and excellent electrical contact between WS$_2$ and W are the main reason for the high activity of WS$_2$/W electrodes reported in this work.

4. Conclusions

In summary, we have developed a straightforward method to prepare vertically-arranged WS$_2$ nanosheets with high surface areas on the oxidized W foil using a bottom-up approach. The direct growth of WS$_2$ on WO$_3$/W minimize the impact of contact resistance between WS$_2$ and electron collection substrate on the HER performance. The ultra-thin WS$_2$ grown on WO$_3$/W heterostructure have abundant exposed stepped WS$_2$ edges as well as defects (S and W vacancy) on the basal plane for HER. This vertically arranged WS$_2$ nanosheets as electrocatalyst exhibits outstanding HER activity with an onset overpotential of as small as approximately 30 mV, a low Tafel slope of 45.5 mV/dec, an overpotential of 108 mV to achieve 10 mA/cm^2, and excellent stability. This synthesis strategy of WS$_2$ nanosheets paves the way for developing more efficient transition metal dichalcogenide catalysts for HER.

Appendix A. Supplementary data

Supplementary material related to this article can be found, in the online version, at doi:https://doi.org/10.1016/j.apcatb.2018.11.042.

References

[1] M.S. Dresselhaus, I.L. Thomas, Alternative energy technologies, Nature 414 (2001) 332–337.
[2] J.O.M. Bockris, The origin of ideas on a hydrogen economy and its solution to the decay of the environment, Int. J. Hydrogen Energy 27 (2002) 731–740.
[3] M. Gratzel, Photoelectrochemical cells, Nature 414 (2001) 338–344.
[4] T.R. Cook, D.K. Dogutan, S.Y. Reece, Y. Surendranath, T.S. Teets, D.G. Nocera, Solar energy supply and storage for the legacy and non legacy worlds, Chem. Rev. 110 (2010) 6474–6502.
[5] I.E.L. Stephens, I. Chorkendorff, Minimizing the use of platinum in hydrogen-evolving electrodes, Angew. Chem. Int. Ed. 50 (2011) 1476–1477.
[6] D.V. Esposito, S.T. Hunt, A.L. Stottlemyer, K.D. Dobson, B.E. McCandless, R.W. Birkmire, J.G. Chen, Low-cost hydrogen-evolution catalysts based on mono-layer platinum on tungsten monocarbide substrates, Angew. Chem. Int. Ed. 49 (2010) 9859–9862.
[7] E. Casado-Rivera, D.J. Volpe, L. Alden, C. Lind, C. Downie, T. Vazquez-Alvarez, A.C.D. Angelo, F.J. DiSalvo, H.D. Abruna, Electrocatalytic activity of ordered in-termetallic phases for fuel cell applications, J. Am. Chem. Soc. 126 (2004) 4043–4049.
[8] J. Greeley, T.F. Jaramillo, J. Bonde, I.B. Chorkendorff, J.K. Norskov, Computational high-throughput screening of electrocatalytic materials for hydrogen evolution, Nat. Mater. 5 (2006) 909–913.
[9] J.K. Norskov, T. Bligaard, J. Rossmeisl, C.H. Christensen, Towards the computa-tional design of solid catalysts, Nat. Chem. 1 (2009) 37–46.
[10] A. Le Goff, V. Artero, B. Jousselme, P.D. Tran, N. Guillet, R. Metaye, A. Fihri, S. Palacin, M. Fontecave, From hydrogenases to noble metal-free catalytic nano-materials for H$_2$ production and uptake, Science 326 (2009) 1384–1387.
[11] M.L. Helm, M.P. Stewart, R.M. Bullock, M.R. DuBois, D.L. DuBois, A synthetic nickel electrocatalyst with a turnover frequency above 100,000 s(-1) for H$_2$ production, Science 333 (2011) 863–866.
[12] T.F. Jaramillo, K.P. Jorgensen, J. Bonde, J.H. Nielsen, S. Horch, I. Chorkendorff,

Identification of active edge sites for electrochemical H$_2$ evolution from MoS$_2$ nanocatalysts, Science 317 (2007) 100–102.

[13] H.I. Karunadasa, E. Montalvo, Y. Sun, M. Majda, J.R. Long, C.J. Chang, A molecular MoS$_2$ edge site mimic for catalytic hydrogen generation, Science 335 (2012) 698–702.

[14] M. Chhowalla, H.S. Shin, G. Eda, L.J. Li, K.P. Loh, H. Zhang, The chemistry of two-dimensional layered transition metal dichalcogenide nanosheets, Nat. Chem. 5 (2013) 263–275.

[15] J. Li, J. Kang, Q. Cai, W. Hong, C. Jian, W. Liu, K. Banerjee, Boosting hydrogen evolution performance of MoS$_2$ by band structure engineering, Adv. Mater. Interfaces 4 (2017) 1700303.

[16] K. Xu, F. Wang, Z. Wang, X. Zhan, Q. Wang, Z. Cheng, M. Safdar, J. He, Component-controllable WS$_{2(1-x)}$Se$_{2x}$ nanotubes for efficient hydrogen evolution reaction, ACS Nano 8 (2014) 8468–8476.

[17] F. Wang, J. Li, F. Wang, T.A. Shifa, Z. Cheng, Z. Wang, K. Xu, X. Zhan, Q. Wang, Y. Huang, C. Jiang, J. He, Enhanced electrochemical H$_2$ evolution by few-layered metallic WS$_{2(1-x)}$Se$_{2x}$ nanoribbons, Adv. Funct. Mater. 25 (2015) 6077–6083.

[18] H. Zhou, F. Yu, J. Sun, H. Zhu, I.K. Mishra, S. Chen, Z. Reif, Highly efficient hydrogen evolution from edge-oriented WS$_{2(1-x)}$Se$_{2x}$ particles on three-dimensional porous NiSe$_2$ foam, Nano Lett. 16 (2016) 7604–7609.

[19] A. Zak, Y. Feldman, V. Lyakhovitskaya, G. Leitus, R. Popovitz-Biro, E. Wachtel, H. Cohen, S. Reich, R. Tenne, Alkali metal intercalated fullerene-like MS$_2$ (M=W, Mo) nanoparticles and their properties, J. Am. Chem. Soc. 124 (2002) 4747–4758.

[20] J. Lin, Z. Peng, G. Wang, D. Zakhidov, E. Larios, M.J. Yacaman, J.M. Tour, Enhanced electrocatalysis for hydrogen evolution reactions from WS$_2$ nanoribbons, Adv. Energy Mater. 4 (2014) 1301875.

[21] D. Voiry, H. Yamaguchi, J. Li, R. Silva, D.C.B. Alves, T. Fujita, M. Chen, T. Asefa, V.B. Shenoy, G. Eda, M. Chhowalla, Enhanced catalytic activity in strained chemically exfoliated WS$_2$ nanosheets for hydrogen evolution, Nat. Mater. 12 (2013) 850–855.

[22] L. Cheng, W.J. Huang, Q.F. Gong, C.H. Liu, Z. Liu, Y.G. Li, H.J. Dai, Ultrathin WS$_2$ nanoflakes as a High-performance electrocatalyst for the hydrogen evolution reaction, Angew. Chem. Int. Ed. 53 (2014) 7860–7863.

[23] J.J. Duan, S. Chen, B.A. Chambers, G.G. Andersson, S.Z. Qiao, 3D WS$_2$ nanolayers@ Heteroatom-doped graphene films as hydrogen evolution catalyst electrodes, Adv. Mater. 27 (2015) 4234–4241.

[24] M.A. Lukowski, A.S. Daniel, C.R. English, F. Meng, A. Forticaux, R.J. Hamers, S. Jin, Highly active hydrogen evolution catalysis from metallic WS$_2$ nanosheets, Energy Environ. Sci. 7 (2014) 2608–2613.

[25] Y. Yang, H. Fei, G. Ruan, Y. Li, J.M. Tour, Vertically aligned WS$_2$ nanosheets for water splitting, Adv. Funct. Mater. 25 (2015) 6199–6204.

[26] H. Zhou, F. Yu, J. Sun, R. He, Y. Wang, C.F. Guo, F. Wang, Y. Lan, Z. Ren, S. Chen, Highly active and durable self-standing WS$_2$/graphene hybrid catalysts for the hydrogen evolution reaction, J. Mater. Chem. A. 4 (2016) 9472–9476.

[27] X. Wang, X. Gan, T. Hu, K. Fujisawa, Y. Lei, Z. Lin, B. Xu, Z.H. Huang, F. Kang, M. Terrones, R. Lv, Noble-metal-free hybrid membranes for highly efficient hydrogen evolution, Adv. Mater. 29 (2017) 1603617.

[28] T.A. Shifa, F. Wang, K. Liu, Z. Cheng, K. Xu, Z. Wang, X. Zhan, C. Jiang, J. He, Efficient catalysis of hydrogen evolution reaction from WS$_{2(1-x)}$P$_{2x}$ nanoribbons, Small 13 (2017) 1603706.

[29] T.A. Shifa, F. Wang, Z. Cheng, X. Zhan, Z. Wang, K. Liu, M. Safdar, L. Sun, J. He, A vertical-oriented WS$_2$ nanosheet sensitized by graphene: an advanced electrocatalyst for hydrogen evolution reaction, Nanoscale 7 (2015) 14760–14765.

[30] J. Barthel, Dr. Probe: a software for high-resolution STEM image simulation, Ultramicroscopy 193 (2018) 1–11.

[31] R.F. Garcia-Sanchez, T. Ahmido, D. Casimir, S. Baliga, P. Misra, Thermal effects associated with the Raman spectroscopy of WO$_3$ gas-sensor materials, J. Phys. Chem. A. 117 (2013) 13825–13831.

[32] S.S. Chan, I.E. Wachs, L.L. Murrell, N.C. Dispenziere, Laser Raman characterization of tungsten oxide supported on alumina: influence of calcination temperatures, J. Catal. 92 (1985) 1–10.

[33] T. Sekine, T. Nakashizu, K. Toyoda, K. Uchinokura, E. Matsuura, Raman scattering in layered compound 2H-WS$_2$, Solid State Commun. 35 (1980) 371–373.

[34] S. Jeong, D. Yoo, M. Ahn, P. Miro, T. Heine, J. Cheon, Tandem intercalation strategy for single-layer nanosheets as an effective alternative to conventional exfoliation processes, Nat. Commun. 6 (2015) 5763.

[35] A. Berkdemir, H.R. Gutierrez, A.R. Botello-Mendez, N. Perea-Lopez, A.L. Elias, C.-I. Chia, B. Wang, V.H. Crespi, F. Lopez-Urias, J.-C. Charlier, H. Terrones, M. Terrones, Identification of individual and few layers of WS$_2$ using raman spectroscopy, Sci. Rep. 3 (2013) 1755.

[36] J.-G. Song, J. Park, W. Lee, T. Choi, H. Jung, C.W. Lee, S.-H. Hwang, J.M. Myoung, J.-H. Jung, S.-H. Kim, C. Lansalot-Matras, H. Kim, layer-controlled, wafer-scale, and conformal synthesis of tungsten disulfide nanosheets using atomic layer deposition, ACS Nano 7 (2013) 11333–11340.

[37] L. Yang, X. Zhu, S. Xiong, X. Wu, Y. Shan, P.K. Chu, Synergistic WO$_3$ center dot 2H(2)O nanoplates/WS$_2$ hybrid catalysts for high-efficiency hydrogen evolution, ACS Appl. Mater. Interfaces 8 (2016) 13966–13972.

[38] J. Kibsgaard, Z. Chen, B.N. Reinecke, T.F. Jaramillo, Engineering the surface structure of MoS$_2$ to preferentially expose active edge sites for electrocatalysis, Nat. Mater. 11 (2012) 963–969.

[39] J.D. Benck, Z. Chen, L.Y. Kuritzky, A.J. Forman, T.F. Jaramillo, Amorphous molybdenum sulfide catalysts for electrochemical hydrogen production: insights into the origin of their catalytic activity, ACS Catal. 2 (2012) 1916–1923.

[40] A. Sengupta, On the junction physics of schottky contact of (10,10) MX$_2$ (MoS$_2$, WS$_2$) nanotube and (10,10) carbon nanotube (CNT): an atomistic study, Appl. Phys. A. 123 (2017) 227.

[41] R.S. Mulliken, Electronic population analysis on LCAO-MO molecular wave functions. I, J. Chem. Phys. 23 (1955) 1833–1840.